Metal-doping of $La_{5.4}MoO_{11.1}$ proton conductors: impact on the structure and electrical properties

Adrián López-Vergara[1], José M. Porras-Vázquez[1,*], Einar Vøllestad[2], Jesús Canales-Vazquez[3], Enrique R. Losilla[1], David Marrero-López[4]

[1] Universidad de Málaga, Dpto. de Química Inorgánica, Cristalografía y Mineralogía, 29071-Málaga, Spain.

[2] University of Oslo, Department of Chemistry, Centre for Materials Science and Nanotechnology, FERMiO, Gaustadalleen 21, 0349 Oslo, Norway

[3] Renewable Energy Research Institute, University of Castilla-La Mancha, 02071-Albacete, Spain

[4] Universidad de Málaga, Dpto. de Física Aplicada I, 29071-Málaga, Spain.

KEYWORDS. Lanthanum molybdate, Nb-doping, polymorphism, mixed ionic-electronic conductor, proton conductivity.

ABSTRACT: $La_{5.4}MoO_{11.1}$ proton conductors with different metal doping (Ca^{2+}, Sr^{2+}, Ba^{2+}, Ti^{4+}, Zr^{4+} and Nb^{5+}) have been prepared and structurally and electrically characterized. Different polymorphs are stabilized depending on the doping and cooling rate used during the synthesis process. The most interesting results are obtained for Nb-doping, $La_{5.4}Mo_{1-x}Nb_xO_{11.1-x/2}$, where single compounds are obtained in the compositional range $0 \leq x \leq 0.2$. These materials are fully characterized by structural techniques such as X-ray and neutron powder diffraction and transmission electron microscopy, which independently confirm the changes of polymorphism. Scanning electron microscopy and impedance spectroscopy measurements in dry/wet gases (N_2, O_2, and 5% H_2–Ar) showed an enhancement of the sinterability and electrical properties of the materials after Nb-doping. Conductivity measurements under very reducing conditions revealed that these materials are mixed ionic-electronic conductors, making them potential candidates for hydrogen separation membranes.

1. INTRODUCTION

Lanthanum tungstates ($La_{6-x}WO_{12-\delta}$) are drawing attention as candidates for hydrogen separation membranes, due to their high ambipolar proton and electronic conductivity and stability in CO_2 and sulfur-containing atmospheres,[1–4] unlike the state-of-the-art proton conductors based on $BaCeO_{3-\delta}$, which exhibit poor stability towards CO_2 due to Ba basicity.[5–7] Moreover, lanthanum tungstates display slow cation diffusivities compared to traditional mixed conducting oxides, leading to an enhanced kinetic stability towards demixing or decomposition during operation.[8,9]

In recent years, lanthanum tungstates have been doped with molybdenum with the goal of increasing the electronic conductivity due to the higher reducibility of molybdenum compared to tungsten.[10–12] Mo-doping improves the hydrogen fluxes compared to the undoped compound, where the best results were obtained by Chen *et al.*[11] for hollow-fiber membranes of $La_{5.6}W_{0.6}Mo_{0.4}O_{11.4}$. Nb-doping also leads to an enhancement of the overall conductivity and hydrogen permeation.[13,14] Other substitutions, such as Ti^{4+}, Zr^{4+}, Al^{3+} and alkaline-earth metals have been successfully performed, improving the electrical properties of these materials.[15,16]

On the other hand, $La_{5.5}W_{1-x}Mo_xO_{11.25}$ compounds crystallize with a cubic structure for $x \leq 0.4$, rhombohedral for $0.4 \leq x < 0.8$ and they are mixed compounds for $x > 0.8$.[17] Molybdates with smaller rare-earth cations, $Ln_{6-x}MoO_{12-\delta}$, present different symmetries depending on the ionic radii of *Ln*: cubic fluorite-type for *Ln*=Sm^{3+}, Gd^{3+} and Dy^{3+} (s.g. $Fm\bar{3}m$) and a cubic bixbyite-type for *Ln*= Ho^{3+}, Er^{3+}, Tm^{3+}, Yb^{3+} and Lu^{3+} (s.g. $Ia\bar{3}$).[18–20] Moreover, to the best of our knowledge, only Zr^{4+}-doping have been investigated in these materials, $Ln_{6-x}Zr_xMoO_{12-\delta}$ (*Ln*= La^{3+}, Nd^{3+}, Sm^{3+} and Dy^{3+}).[21–23]

Recently, it has been carried out a comprehensive study of the effect of the synthesis conditions on the structure and electrical properties of $La_{6-x}MoO_{12-\delta}$ ($0 \leq x \leq 0.8$) series.[24] Different polymorphs are stabilized at room temperature depending on the cooling conditions: a single cubic fluorite structure is isolated from the sudden cooling of the samples (quenching), whereas slower cooling rates (50 and 0.5 ºC min^{-1}) led to two different polymorphs with 7×7×1 and 5×5×1 superstructures with rhombohedral unit basic cells, which will be referred in the present work as R1 and R2, respectively. The electrical characterization showed that all samples are proton conductors in wet atmospheres; however, they are mixed ionic-electronic conductors under reducing conditions.

The aim of this work is to carry out a thorough study of the effect of metal-doping, i.e. Ca^{2+}, Sr^{2+}, Ba^{2+}, Ti^{4+}, Zr^{4+} and Nb^{5+}, on the polymorphism and electrical properties of $La_{5.4}MoO_{11.1}$-based materials. X-ray powder diffraction (XRPD), neutron powder diffraction (NPD), and scanning and transmission electron microscopy (SEM and TEM) have been employed to study the structural characteristics of the materials. The different contributions to the overall conductivity have been determined by impedance spectroscopy in different dry/wet atmospheres and as a function of the oxygen partial pressure.

2. EXPERIMENTAL SECTION

2.1. Synthesis.

Samples with composition $La_{5.4}Mo_{0.9}A_{0.1}O_{12-\delta}$ (A = Ti, Zr and Nb) and $La_{5.3}B_{0.1}MoO_{11.05}$ (B = Ca, Sr and Ba) were prepared by the freeze-drying precursor method, following the procedure described in a previous work for related materials.[16] The starting reagents were: La_2O_3 (99.99%, Aldrich), MoO_3 (99.5%, Aldrich), $CaCO_3$ (99%, Alfa Aesar), $SrCO_3$ (99.99%, Alfa Aesar), $BaCO_3$ (99%, Alfa Aesar), $Ti[OCH(CH_3)_2]_4$ (99%, Aldrich), $ZrO(NO_3)_2{\cdot}6H_2O$ (99% Aldrich), and $Nb(HC_2O_4)_5{\cdot}H_2C_2O_4$ (97% ABCR). The precursor solutions were prepared by dissolving separately La_2O_3 and alkaline-earth carbonates in diluted nitric acid, MoO_3 in diluted ammonia, $Ti[OCH(CH_3)_2]_4$ in ethanol, and $ZrO(NO_3)_2{\cdot}6H_2O$ and $Nb(HC_2O_4)_5{\cdot}H_2C_2O_4$ in distilled water. An ethylenediaminetetraacetic acid solution (EDTA, 99.99%, Aldrich) was added as a complexing agent in a molar ratio 1:1 with respect to the sum of the metal salts. The different cation solutions were mixed in stoichiometric amounts under stirring, obtaining transparent solutions with a concentration of 0.1 mol L^{-1} and pH~7. The solutions were frozen into liquid nitrogen and then dehydrated in a Scanvac Coolsafe freeze-dryer for 2 days. The dried precursor powders were firstly calcined at 300 ºC for combustion and then at 800 ºC for 1 h to remove the carbon species. The resulting powders were compacted into pellets with 10 and 1 mm of diameter and thickness, respectively, placed onto platinum plates and sintered at 1500 ºC for 1 hour. Then, in order to compare the results with those obtained in a previous work, the pellets were cooled down at three different rates by using a low capacity furnace: quenching (fast cooling at room temperature), 50 and 0.5 ºC min^{-1}.[24] The obtained pellets were ground into powder for further characterization. Finally, the powder samples were annealed between room temperature and 800 ºC for several days to check the phase stability. Hereafter, all samples are labelled as M_x_T, where M is the dopant cation, x is the dopant content and T the cooling rate used.

2.2. Structural and thermal characterization

All samples were analyzed by laboratory X-ray powder diffraction (XRPD) by using a PANalytical Empyrean diffractometer with $CuK\alpha_{1,2}$ radiation. The acquisition time was approximately 4 h over the 2θ angular range of 10-120º. The phase identification and structural analysis were performed using the X'Pert HighScore Plus and GSAS software.[25,26]

Time of flight neutron powder diffraction (TOF-NPD) data were recorded on the Gem Xpress diffractometer at the ISIS pulsed spallation source (Rutherford Appleton Laboratory, UK). 6 g of powdered samples were loaded into 6 mm diameter vanadium cans and the data were collected at ambient temperature. The overall measurement time was ~2 h. Only those banks with the best signal/noise ratio (4, 5 and 6) were analyzed using the GSAS suite of programs.

The crystal structure of the materials was also investigated by selected area electron diffraction (SAED) and high-resolution transmission electron microscopy (HRTEM). The specimens were prepared by grinding the powders in acetone and the resulting suspension was deposited onto a holey carbon-coated copper support grid. The measurements were performed on a Jeol JEM 2100 electron microscope operating at 200 kV. TEM images were analyzed using the Digital Micrograph™ software.[27]

The microstructure of the ceramics was observed by scanning electron microscopy (SEM) (Jeol JSM-6490LV), combined with energy dispersive spectroscopy (EDS) (Oxford Instruments). The grain size of the dense pellets was estimated from the SEM micrographs, using the linear intercept method with the Estereologia software.[28] Different images were analyzed to obtain the grain size distribution and average grain size.

2.3. Electrical characterization

Impedance spectra were acquired using a frequency response analyzer (Solartron 1260 FRA) in dry and wet (2 vol.% H_2O) gases of N_2, O_2 and 5% H_2-Ar. The data were collected in the 0.01 Hz to 1 MHz frequency range with an ac perturbation of 100 mV on cooling from 800 to 200 °C and a dwell time of 30 min at each measurement temperature. For the measurements in 5% H_2-Ar the samples were previously reduced for one day at 800 ºC and the data were acquired on cooling with a dwell time between 30 min and 1 h. The data were simulated by equivalent circuit models using the ZView program.[29] Pt current collectors were formed by coating the pellet surfaces with Pt-ink (METALOR® 6082) and then fired at 800 ºC for 1 h in air.

The dependence of the conductivity with the oxygen partial pressure (pO_2) was studied from oxidizing (100% O_2) to very reducing conditions (100% H_2) at a constant water partial pressure (pH_2O) of ~2.5 vol.% H_2O in a ProboStat cell (NorECs, Norway) by the 2-point 4-wire method.[30] The conductivity was monitored versus time at each new set of conditions to ensure that equilibrium was achieved before taking a measurement.

3. RESULTS AND DISCUSSION

3.1. Single phase existence on metal doping

Substitutions on the molybdenum ($La_{5.4}Mo_{0.9}A_{0.1}O_{12-\delta}$) and lanthanum ($La_{5.3}B_{0.1}MoO_{11.05}$) sites were firstly evaluated using the same synthetic conditions reported for the

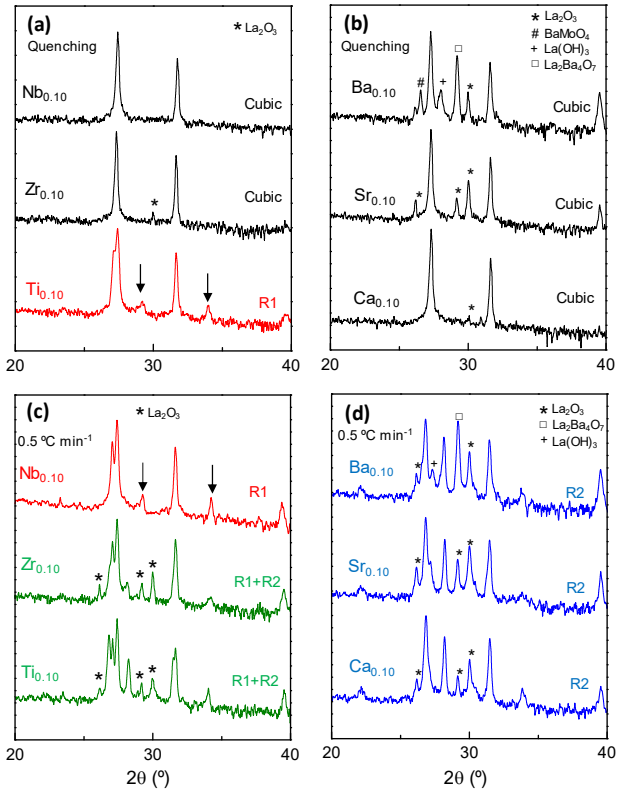

Figure 1. XRPD patterns for $La_{5.4}Mo_{0.9}A_{0.1}O_{12-\delta}$ (B = Ti, Zr and Nb) and $La_{5.3}B_{0.1}MoO_{11.05}$ (A = Ca, Sr and Ba) heated at 1500 ºC and cooled down by (a,b) quenching and at (c,d) 0.5 ºC min^{-1}. Secondary phases are labelled as well as the polymorphism of the main lanthanum molybdate phase. Superstructure peaks are labelled with arrows for single-phase samples. Intensities are given in logarithmic scale for better visualization of the lower intensity peaks.

undoped compounds.[24] The samples prepared by quenching crystallize with a cubic ($Ca_{0.1}$, $Sr_{0.1}$, $Ba_{0.1}$, $Zr_{0.1}$ and $Nb_{0.1}$) or rhombohedral ($Ti_{0.1}$) symmetry (Fig. 1a and b and Table S1). However, only $Nb_{0.1}$ and $Ti_{0.1}$ are single-phase compounds, the rest of the compositions exhibit secondary phases, identified as La_2O_3, $BaMoO_4$, $La(OH)_3$ and $La_2Ba_4O_7$.

It should be noted that the amount of secondary phases increases with the ionic radii of the alkaline-earth metal, in the order $Ba_{0.1}$ > $Sr_{0.1}$ > $Ca_{0.1}$. To the best of our knowledge, only Zr^{4+} has been reported as a successful dopant for rare-earth molybdates. Zr^{4+}(0.84 Å) is significantly smaller than La^{3+}(1.16 Å), Sm^{3+}(1.08 Å) and Dy^{3+}(1.03 Å).[21] Therefore, doping in the lanthanum position for Ca^{2+}(1.12 Å), Sr^{2+}(1.26 Å) and Ba^{2+}(1.42 Å) is not possible. It should be noticed that this behavior is different to that reported for lanthanum tungstates, $La_{5.35}M_{0.1}WO_{11.125}$ (M = Ca^{2+} and Sr^{2+}), where all the samples were single phase compounds.[15]

The cubic polymorph is not stabilized for any composition when the samples are prepared at the lowest cooling rate (0.5 ºC min^{-1}) (Fig. 1c and 1d and Table S1), and only $Nb_{0.10}$_0.5, with a rhombohedral R1-type symmetry, is obtained as a single-phase. $Ti_{0.10}$_0.5 and $Zr_{0.10}$_0.5 are a mixture of R1 and R2-type polymorphs, containing minor segregations of La_2O_3. This behavior clearly indicates that metal-doping on the molybdenum position trends to stabilize the R1 polymorph when a low cooling rate is used, but only Nb-doping leads to pure compounds. Similar results are obtained for a cooling rate of 50 ºC min^{-1}, where only $Nb_{0.1}$ and $Ti_{0.1}$ are single-phase compounds with a R1 symmetry (Table S1).

Since Nb is the only dopant with beneficial effects on the structural properties of $La_{5.4}MoO_{11.1}$ without secondary phases segregations or mixture of polymorphs, samples with different Nb-content, $La_{5.4}Mo_{1-x}Nb_xO_{11.1-x/2}$ (x = 0, 0.05, 0.10, 0.15 and 0.20), were prepared in order to gain a better understanding of the effect of Nb-doping on the structural and electrical properties.

XRPD patterns for $La_{5.4}Mo_{1-x}Nb_xO_{11.1-x/2}$ prepared by quenching are showed in Fig. S1a. All samples are single phase for x≤0.2 and present a simple cubic fluorite-type structure. For x>0.25, small segregations of La_2O_3 are observed in the XRPD patterns, indicating that the solubility limit of Nb in $La_{5.4}Mo_{1-x}Nb_xO_{11.1-x/2}$ series, under the synthetic conditions used, is close to x=0.2. In the case of the samples obtained at a cooling rate of 50 ºC min^{-1}, all compounds crystallize with a rhombohedral R1-type structure (Fig. S1b).

A different behavior is observed for samples obtained at 0.5 ºC min^{-1}. The undoped compound is a single-phase with R2-structure (Fig. S1c) and $Nb_{0.1}$_0.5 crystallizes with a R1-structure. Lower Nb-content (x≤0.05) leads to a mixture of R1 and R2 polymorphs, whereas for x>0.1, the materials crystallize with a R1-type structure but exhibit minor segregations of La_2O_3. It is worth mentioning that changes in polymorphism have been also reported for other lanthanum molybdates, such as $La_2Mo_2O_9$, after Nb-doping or the modification of the synthesis-sintering conditions, leading to the stabilization of higher symmetry forms.[31-32]

3.2. Structural analysis of the Nb-doped compounds

As previously commented, Nb_x_0.5 and Nb_x_50 series crystallize with complex rhombohedral superstructures, similar to that of $La_{5.4}MoO_{11.1}$ cooled down at 50 ºC min^{-1}.[24] Since complete structural models are not available in the literature, only the basic unit cell parameters were determined by a Le Bail analysis of the XRPD data. An example of the fitting for $Nb_{0.1}$_0.5 is shown in Fig. 2a, where the small diffraction peaks, attributed to superstructure reflections, are not indexed.

Nb_x_Q series is studied by a combined Rietveld refinement of X-ray and time of flight-neutron powder diffraction data, using a single fluorite-type structure with a $Fm\bar{3}m$ space group as starting structural model.[24] Occupancy factors were initially set to the nominal stoichiometry, where La, Mo and Nb were located in the same crystallographic position and their isotropic displacement parameters constrained to be the same. Parameters such as unit cell, scale factor, background and peak shape coefficients and isotropic displacement parameters were refined.

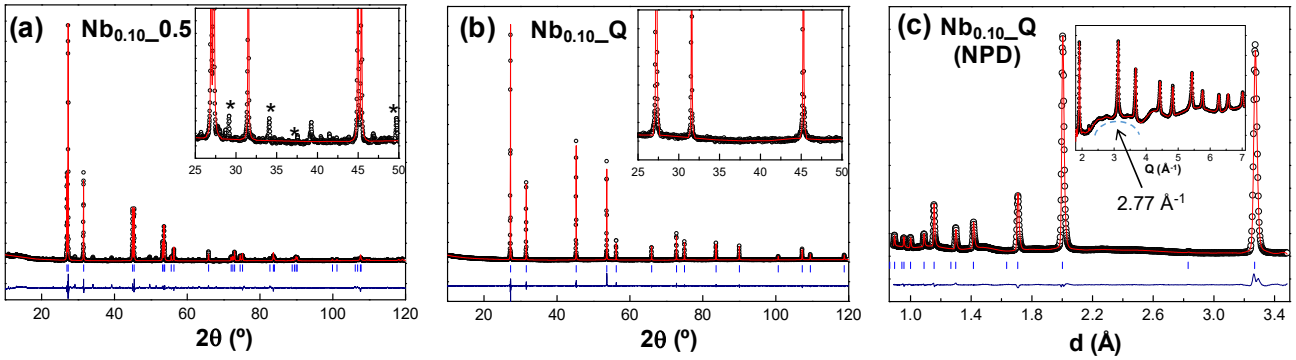

Figure 2. XRPD Le Bail plot for rhombohedral (a) $Nb_{0.10}$_0.5. Rietveld plot for (b) cubic $Nb_{0.10}$_Q. (c) TOF-NPD Rietveld plot for $Nb_{0.10}$_Q (bank 4). The inset of (c) shows the TOF-NPD pattern as a function of Q. [Observed data (circles), calculated pattern (continuous line), and difference curve (bottom)].

In Figure 2b-c and Tables S2 and S3 it can be seen that the refinements are quite satisfactory, with low disagreement factors, R_F and R_{wp} values vary between 2-3 (2-4) and 5-8 (3-4), for XRPD and TOF-NPD (italics) data, respectively, confirming that all quenched samples crystallize in a single cubic fluorite structure. Similar results are obtained for the remaining samples (Table S3). Moreover, occupancy factors were refined freely, without any constraint, and La, Mo and Nb remained practically unaltered from the nominal values, indicating that the experimental stoichiometry is very close to the nominal one. Therefore, cation occupancy factors were fixed to the nominal values (Table S3). Refinement of the oxygen occupancy factors yields to higher concentration of oxygen vacancies with increasing of Nb-doping as expected (Table S3).

TOF-NPD patterns for the quenched samples show a significant undulation of the background (Fig. 2c). This behavior has already been reported for other oxide ion conductors, such as $La_2Mo_2O_{9-\delta}$, $Bi_{26}Mo_{10}O_{69-\delta}$ and Bi_2O_3-based materials,[33–37] and is ascribed to a contribution of local static structural disorder in the anionic sublattice, caused by fast oxide ion diffusion, to the elastic diffuse scattering.[38,39] The nature of this disorder can be ascertained by the first undulation maximum of the background, where a very significant contribution to its intensity comes from the static structural disorder. This intensity can be expressed by the Debye formula,[36] where the maximum is achieved for:

$$Q_{\max} = \frac{2\pi \times 1.23}{d_{\max}}$$

where d_{max} is a preferred pair distance. In the inset of Figure 2c it can be seen that for $Nb_{0.10}$_Q the maximum is about 2.77 $Å^{-1}$, corresponding to $d_{max} \approx 2.79$ Å, and close to the experimental O-O distances, 2.83 Å, of the 8-fold coordination of La, Mo and Nb. Similar pair distances are obtained for Nb_0_Q and $Nb_{0.20}$_Q. This confirms that the modulation observed in the patterns can be ascribed to the distribution of the oxygen defects. Similar results are reported in the literature for related molybdates, i.e. Q_{max} of 2.75 and 2.8 $Å^{-1}$, for $Bi_{26}Mo_{10}O_{69}$ and $La_2Mo_2O_9$, respectively.[34,36]

The unit cell volume of the quenched samples decreases linearly along the series, according to the Vegard's law, due to the smaller ionic radii of Nb^{5+}(0.74 Å) in an 8-fold coordination, in comparison to those of La^{3+}(1.16 Å) and Mo^{6+}(1.02 Å) in the same environment (Figure S2). It has to be noted that the ionic radii of Mo^{6+} in 8-fold coordination is not reported in Shannon´s database,[40] therefore it has been estimated from the Mo-O distances of several molybdenum-containing compounds: $La_{2.4}Mo_{1.6}O_8$ (ICSD 27006), $Ho_2MoO_{4.8}$ (ICSD 261709), $Bi_{3.2}Mo_{0.8}O_{7.5}$ (ICSD 38357) and Mo_3O (ICSD 15903), all of them with a $Fm\bar{3}m$ space group.[41–43]

A similar trend is observed for Nb_x_50 series, as the unit cell volume decreases with increasing Nb-doping with the exception of the undoped compound that exhibits a value

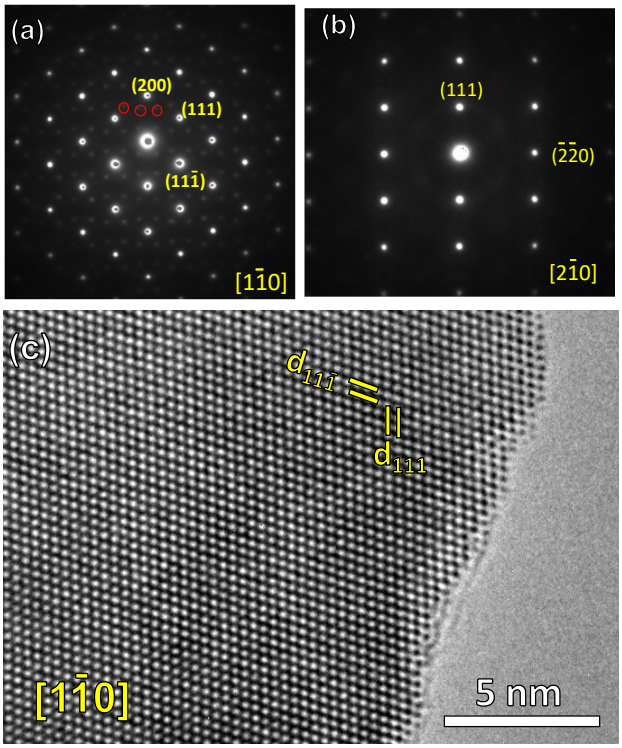

Figure 3. SAED patterns of $Nb_{0.1}$_Q in (a) [1-10] and (b) [2-10] zone axes. Red circles indicate weak satellite reflections due to structure modulation. (c) HRTEM image in the [1-10] zone axis.

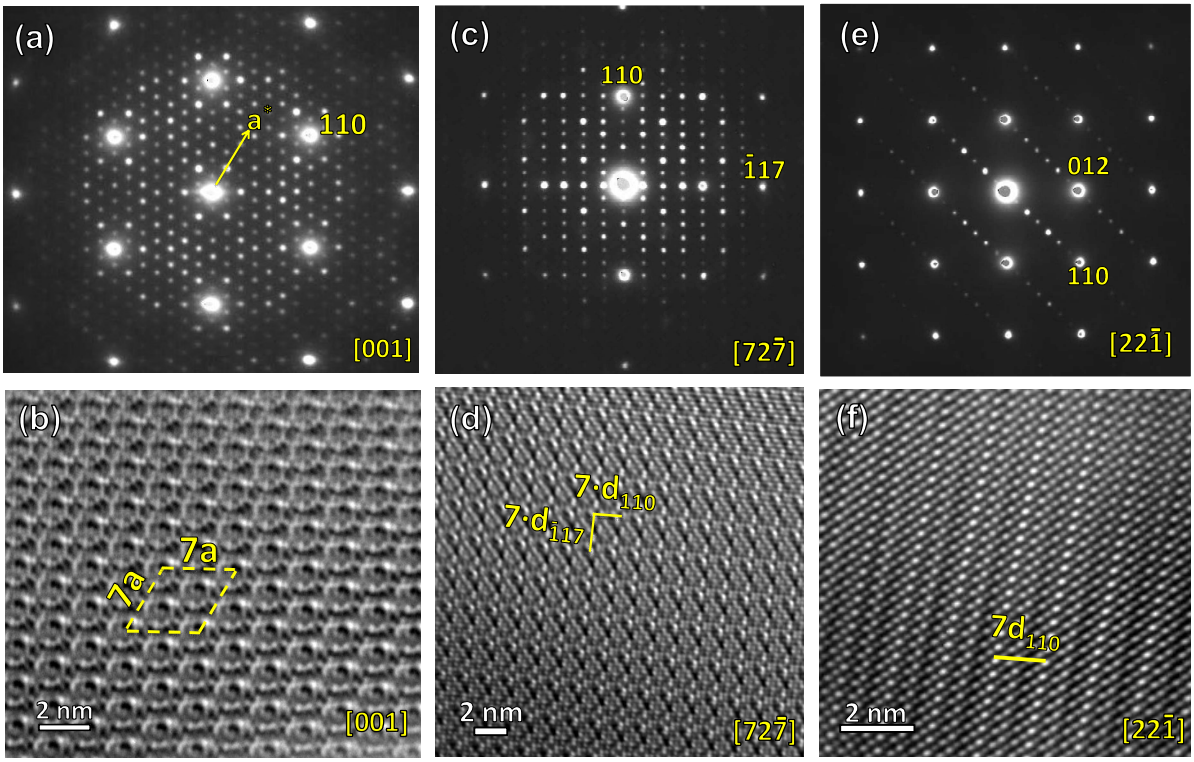

Figure 4. SAED patterns and HRTEM images for $Nb_{0.1}$_0.5 in (a,b) [001], (c.d) [72-7] and (e,f) [22-1] zone axes.

somewhat lower than the expected one. (Figure S2). In contrast, this linear dependence is not observed for the samples prepared at low cooling rate (0.5 ºC min^{-1}), which can be explained by the structural phase transition from R2 to R1 polymorph with Nb-doping and also the presence of minor secondary phase segregations of La_2O_3 for x≥0.15.

These results indicate that not only the cooling rate has a significant effect on the polymorphism of $La_{6-x}MoO_{12-\delta}$[24] but also the incorporation of different aliovalent dopants, which introduces extrinsic oxide ion vacancies in the lattice, suggesting that the local structure of the different polymorphs is similar and the differences are mainly associated with modifications in the oxygen sublattice as previously observed for related materials, such as the fast ionic conductor $La_2Mo_2O_9$ with a α-monoclinic→β-cubic structural phase transition from a static to a dynamic distribution of the oxygen defects.[45] However, additional measurements are necessary to confirm this hypothesis, such as neutron atomic pair distribution function (PDF) analysis.

3.3. Structural Analysis by TEM

The structure of the materials was further characterized by combined selected area electron diffraction (SAED) and high resolution TEM image. For the quenched sample, the main reflections of the SAEDs could be indexed on the basis of a cubic fluorite-type structure with cell parameter a= 5.67 Å, in agreement with the XRPD and NPD results (Fig. 3a-b). However, certain crystallographic directions show weak satellite reflections, consistent with an incommensurate modulation due to local oxygen ordering as it was observed by the neutron diffraction measurements (Fig. 3a). HRTEM images further confirm the cubic structure of this sample, where the interplanar distances are similar to those obtained by diffraction techniques (Fig. 3c).

SAED patterns for the sample cooled down at 0.5 ºC min^{-1}, $Nb_{0.1}$_0.5, reveal the presence of a superstructure. This is clearly observed in the [001] zone axis (Fig. 4a), where the most intense reflections correspond to a basic rhombohedral cell with a=b=4.10 Å and c= 9.52 Å, and the weak reflections indicate that the real cell is a 7a×7a supercell. This is further confirmed by the HRTEM image of Fig. 4b, where this supercell is clearly visible. Moreover, along the (003) direction no superstructure reflections are observed (Fig. S3), indicating that the superstructure is 7a×7a×c of a basic unit cell. Similar results are observed in different zone axes, Fig 4c and 4e, where the SAEDs are correctly indexed by considering the proposed basic rhombohedral cell. HRTEM images viewed down these zone axes corroborate the results (Fig. 4d and 4f).

3.4. Microstructural and electrical characterization

The sintered pellets for all compositions exhibit very high relative density, close to 100%, independently on the cooling process employed (Fig. S4). The quenched samples and those cooled at 50 ºC min^{-1} do not show any evidence of secondary phase segregations in the whole compositional range studied, 0≤x≤0.2, and are chemical and mechanically stable in different atmospheres. In addition, cracks associated with the fast cooling process are not detected.

The samples prepared at 0.5 ºC min^{-1} with Nb-content 0<x≤0.05 are mixture of polymorphs and contain minor segregation of La_2O_3, which hydrate and carbonate in

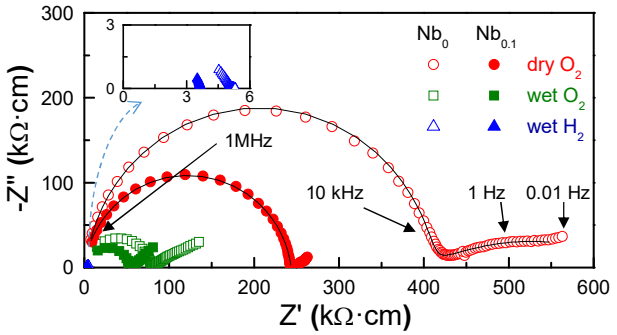

Figure 5. Representative impedance spectra of Nb_0_Q and $Nb_{0.10}$_Q in dry/wet O_2 and wet 5% H_2-Ar gases at 400 ºC.

humidified atmospheres, leading to the mechanical degradation of the pellets after exposing to air for several days. Only $Nb_{0.1}$_0.5 is a single-phase compound and stable in the different environments. The remaining compositions of this series are unstable and they are not electrically characterized.

SEM images reveal that the average grain size increases with Nb-doping. For instance, the grain size diameter for the quenched samples increases from 15.8 to 31.7 μm for Nb_0_Q and $Nb_{0.2}$_Q, respectively. On the other hand, the grain size increases as the cooling rate decreases due to longer dwelling times at high temperature and the consequent grain growth (e.g. 33.5 μm for Nb_0_Q to 54 μm for $Nb_{0.1}$_0.5).

Impedance spectra of the pellets were acquired under several atmospheres in order to study the different contributions to the overall conductivity. Representative impedance spectra plots for $Nb_{0.1}$_Q are shown in Figure 5. All spectra show similar characteristics, independently on the composition, atmosphere and cooling rate employed during the synthesis. Two different processes are distinguished in the spectra; the dominant one at high frequency with a capacitance of ~pF cm^{-1} is associated with the grain interior conduction. The low frequency contribution with higher values of capacitance, ~mF cm^{-1}, is attributed to the electrode response. It should be noticed that the grain boundary contribution is not detected due to the large grain size of the sample and the absence of phase segregations. Hence, the bulk conductivity is predominant in these materials. The impedance spectra were simulated by an equivalent circuit model: $(R_bQ_b)(R_eQ_e)$, where R is a resistance and Q is a pseudo-capacitance; and b and e denote the grain interior and electrode responses, respectively.

The Arrhenius plots show a very significant increase of the conductivity in wet atmospheres at low temperatures (T < 600 ºC) for both the cubic and rhombohedral polymorphs (Fig. 6), due to a significant proton contribution to the overall conductivity as previously observed for the undoped compounds.[24] As expected the proton conductivity decreases as the temperature increases due to the release of water and a reduction in the proton concentration. In particular, above 700 ºC, the conductivity values in dry and wet O_2 gases are similar, indicating that oxide ions are the main mobile species.

For the cubic samples, the overall conductivity increases with Nb-doping due to the generation of extrinsic oxide ion vacancies in the lattice when Mo^{6+} is partially substituted by Nb^{5+} (Fig. S5 and Table S4). The maximum conductivity is observed for x=0.10, with a value of 1.7 mS cm^{-1} at 800 ºC in wet O_2, which is a significant improvement with respect to the undoped compound ~0.71 mS cm^{-1}. A similar trend is observed in the low temperature range (T<600 ºC), where the conductivity is dominated by the proton contribution. Therefore, Nb-doping enhances both oxide ion and proton conductivity in $La_{5.4}MoO_{11.1}$-based compounds up to x = 0.10. An increase of Nb-substitution above x>0.15 leads to an excessive oxygen vacancy concentration in the lattice and their possible association; consequently, no further improvement of the conductivity is observed.[46] A similar trend is observed for the samples cooled down at 50 ºC min^{-1}, where the conductivity maximum is also observed for Nb0.10_50.

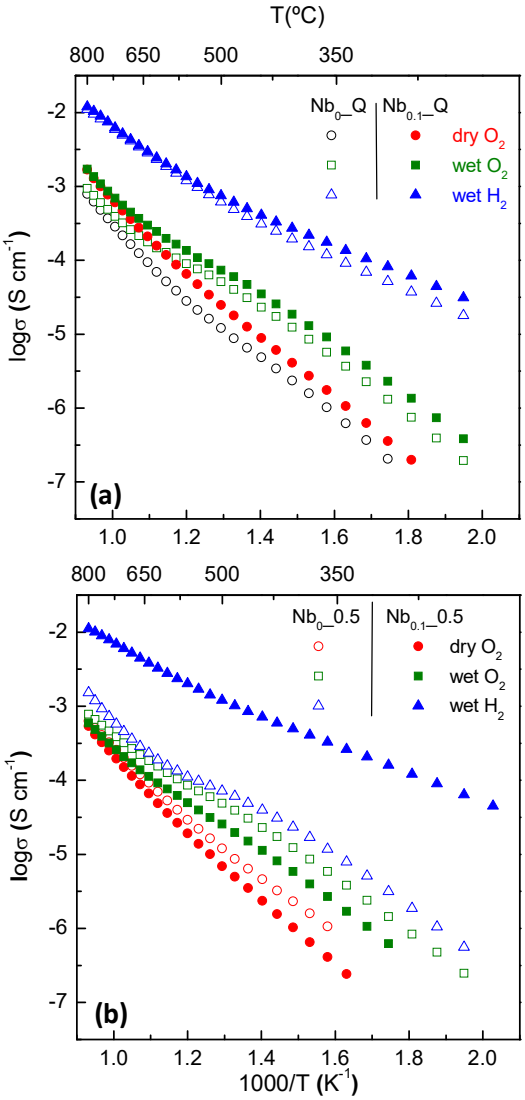

Figure 6. Arrhenius plots of the overall conductivity of Nb_0_Q and $Nb_{0.10}$_Q in dry/wet O_2 and wet 5% H_2-Ar prepared at different cooling rates: quenching and 0.5 ºC/min.

On the other hand, the quenched samples exhibit higher conductivity values than those prepared at low cooling rates, which could be explained by the higher structural symmetry and improved mobility of the charge carriers (Table S3). Regarding the Nb_x_0.5 series, a decrease in the conductivity is observed for $Nb_{0.10}$_0.5 in comparison to the undoped compound (Nb_0_0.5), which is ascribed to the structural change on doping from R2 to R1 polymorphs. No other members of this series were analyzed by impedance spectroscopy due to the segregation of La_2O_3 and the disruptive expansion of the pellets.

Activation energies at low temperatures for all compositions were very similar, with values of ~0.81 eV in dry atmospheres, and ~0.72 eV in wet atmospheres, indicating that Nb-doping does not lead to any change in the proton conduction mechanism. On the other hand, the activation energies increase to 1.33 eV at high temperatures, regardless of the measurement conditions because the conductivity is dominated by the oxide ion conduction.

In reducing atmospheres, the conductivity increases significantly for the different samples, which could be explained by an increase of the n-type electronic conductivity due to the reduction of Mo^{6+} to Mo^{5+} with the consequent loss of lattice oxygen and formation of oxygen vacancies $[V_O^{\bullet\bullet}]$, according to the following relation in the Kröger-Vink notation:

$$2Mo_{Mo}^{x} + O_O^{x} \rightarrow 2Mo'_{Mo} + V_O^{\bullet\bullet} + 1/2O_2 \qquad (1)$$

where the mass action equation is:

$$K_R = \frac{[Mo'_{Mo}]^2[V_O^{\bullet\bullet}]}{[Mo_{Mo}^{x}]^2[O_O^{x}]}(pO_2)^{1/2} \qquad (2)$$

XPS measurements in a previous work confirmed that only a little fraction of Mo^{6+} is reduced to Mo^{5+}, i.e. $[Mo_{Mo}^{x}] >> [Mo'_{Mo}]$ [22]. Moreover, the number of oxygen vacancies created during the reduction process is half of the reduced molybdenum: $[V_O^{\bullet\bullet}] = [Mo'_{Mo}]/2$. Hence, the number of electron charge carriers and the n-type electronic conductivity are proportional to $(pO_2)^{-1/6}$. For Nb_x_Q and Nb_x_50 series the conductivity increases on Nb-doping up to x = 0.10. In the case of Nb_x_0.5, series the conductivity of $Nb_{0.10}$_0.5 is higher than that of Nb_0_0.5, due to the structural change on Nb-doping from R2 to R1 polymorph. As it was discussed in our previous work,[24] the n-type electronic conductivity of the R1 polymorph is higher than that of R2; however, an explanation for this behavior requires a further structural analysis.

The dependence of the conductivity on the oxygen partial pressure (pO_2) shows the typical behavior of a mixed ionic-electronic conductor as can be seen in Figure 7 for $Nb_{0.10}$_0.5. The conductivity increases as pO_2 decreases, indicating that under reducing conditions the n-type electronic conductivity is the main conduction mechanism. In contrast, under oxidizing atmospheres, the conductivity increases slightly with pO_2 indicating the presence of a minor p-type electronic contribution.[47] A very

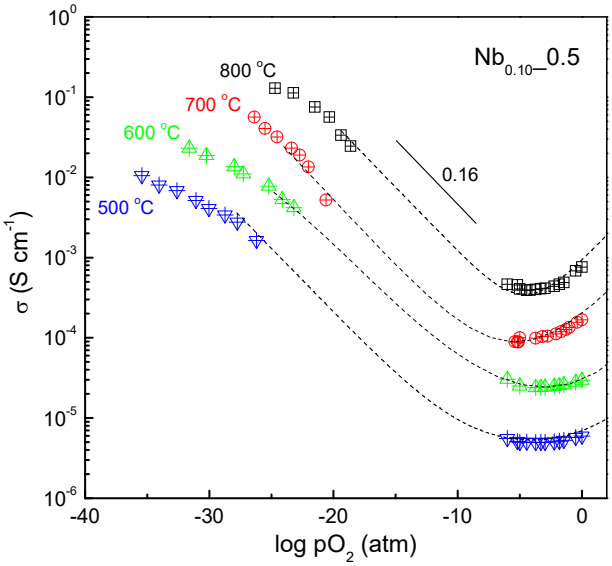

Figure 7. Variation of the overall conductivity as a function of the oxygen partial pressure at 800 °C for $Nb_{0.10}$_0.5. The dashed line is the fitting curve with Eq. 3.

similar behavior is observed for $Nb_{0.10}$_Q and $Nb_{0.10}$_50. The overall conductivity, σ, could be expressed according to the following relation:

$$\sigma = \sigma_i + \sigma_n^o(pO_2)^{-1/6} + \sigma_p^o(pO_2)^{1/6} \qquad (3)$$

where σ_i is the ionic conductivity, and σ_n^o and σ_p^o are the n-type and p-type electronic conductivities at pO_2=1 atm.

It has to be noticed that the p-type electronic contribution is only partially observed at high values of pO_2 and it is not possible to determine the power law dependence: $(pO_2)^n$ (n=1/4 or 1/6). For simplicity, we have assumed a similar behavior for both the p-type and n-type electronic contributions; however, additional experiments, such as ion-blocking, are necessary to study separately the ionic and electronic conductivity.

As can be observed the curves are fitted with Eq. 3, confirming the proposed dependence of the electronic conductivity on the oxygen partial pressure. However, at very low oxygen partial pressures the curves show a different slope, which is not adequately simulated by Eq. 3. This behavior is mainly observed at temperatures below 600 ºC and could be associated with a decrease of the water partial pressure on pO2, and the consequent decrease of ionic conductivity, as previously reported for other proton conducting materials.[48-50] The values of ionic transport numbers for $Nb_{0.10}$_0.5 are estimated from: $t=\sigma_i/\sigma$, taking values of about 0.6 at 600 ºC and 0.3 at 800 ºC at pO_2=1 atm. These values decrease to 0.005 and 0.0025 at 600 and 800 ºC at $pO_2=10^{-25}$ atm, similar to those obtained for the undoped compounds.[24] Hence, these materials are proton conductors under oxidizing and wet conditions; however, they are predominantly n-type electronic conductors under reducing atmospheres. As further work, hydrogen permeability experiments are planned to evaluate the performance of these materials as hydrogen separation membranes.

4. CONCLUSIONS

Metal (Ca^{2+}, Sr^{2+}, Ba^{2+}, Ti^{4+}, Zr^{4+} and Nb^{5+}) doped $La_{5.4}MoO_{11.1}$ samples were synthetized by the freeze-dried precursor method. The ceramics were sintered and cooled down at three different rates: quenching, 50 and 0.5 ºC min^{-1}. XRPD analysis revealed that single-phase compounds with cubic symmetry are only obtained for Nb-doping. Titanium samples are single-phases with a R1 symmetry at fast cooling rates. In addition, a stabilization of a rhombohedral polymorph (R1) is observed at 0.5 ºC min^{-1} for Nb series. TOF-NPD data confirmed the cation stoichiometry of the cubic polymorphs and TEM studies ascertained the polymorphism: a single cubic fluorite and a 7a×7a×c rhombohedral structure, for the samples cooled down by quenching and 0.5 ºC min^{-1}, respectively.

Nb-doping improves the densification and grain growth rate of the samples. In addition, an enhancement of the conductivity is observed due to an increase of the oxide vacancy concentration; however, high dopant content (x>0.1) leads to poorer values of conductivity, possibly due to vacancy defect association. Finally, under very reducing conditions, an important n-type electronic contribution to the conductivity is detected due to the partial reduction of Mo^{6+} to Mo^{5+} with ionic transport numbers at 600 ºC of 0.6 in air and 0.005 in H_2.

ASSOCIATED CONTENT

Additional experiment results, including XRPD patterns, SAED and SEM images, variation of the unit cell volume and conductivity with the Nb content. This material is available free of charge via the Internet at http://pubs.acs.org.

AUTHOR INFORMATION

Corresponding Author

*E-mail address: josema@uma.es (José M. Porras-Vázquez)
Tel: +34 952132022 / +34 616112050.

Author Contributions

The manuscript was written through contributions of all authors. All authors have given approval to the final version of the manuscript.

Funding Sources

This work was supported by MINECO (Ministerio de Economía y Competitividad) through the MAT2016-77648-R research grant (Spain) which is co-funded by FEDER. J.M.P.-V. thanks the University of Málaga for his funding and Young Researcher project. A. L.-V. thanks Junta de Andalucía and the European Social Fund for his Young Researcher Contract (UMAJI35).

ACKNOWLEDGMENT

We would like to thank the ISIS facility for NPD time and Ronald I. Smith for his help with the beamtime proposal.

REFERENCES

(1) Escolástico, S.; Solís, C.; Serra, J. M. Study of hydrogen permeation in $(La_{5/6}Nd_{1/6})_{5.5}WO_{12-\delta}$ membranes. *Solid State Ionics* **2012**, *216*, 31–35.

(2) Gil, V.; Gurauskis, J.; Kjølseth, C.; Wiik K.; Einarsrud, M.-A. Hydrogen permeation in asymmetric $La_{28-x}W_{4+x}O_{54+3x/2}$ membranes. *Int. J. Hydrog. Energy* **2013**, *38*, 3087–3091.

(3) Escolástico, S.; Solís, C.; Scherb, T.; Schumacher, G.; Serra, J. M. Hydrogen separation in $La_{5.5}WO_{11.25-\delta}$ membranes. *J. Membrane Sci.* **2013**, *444*, 276–284.

(4) Gil, V.; Gurauskis, J.; Einarsrud, M.-A. Asymmetric supported dense lanthanum tungstate membranes. *J. Eur. Ceram. Soc.* **2014**, *34*, 3783–3790.

(5) Medvedev, D.; Murashkina, A.; Pikalova, E.; Demin, A.; Podias, A.; Tsiakaras, P. $BaCeO_3$: Materials development, properties and application. *Prog. Mater. Sci.* **2014**, *60*, 72–129.

(6) Tao, Z. T.; Yan, L. T.; Qiao, J. L.; Wang, B. L.; Zhang, L.; Zhang, J. J. A review of advanced proton-conducting materials for hydrogen separation. *Prog. Mater. Sci.* **2015**, *74*, 1–50.

(7) Ruiz-Trejo, E.; Irvine, J. T. S. Ceramic proton conducting membranes for the electrochemical production of syngas. *Solid State Ion.* **2012**, *216*, 36–40.

(8) Vøllestad, E.; Teusner, M.; De Souza, R. A.; Haugsrud, R. Diffusion of Nd and Mo in lanthanum tungsten oxide. *Solid State Ion.* **2015**, *274*, 128–133.

(9) Vøllestad, E.; Norby, T.; Haugsrud, R. Inter-diffusion in lanthanum tungsten oxide. *Solid State Ion.* **2013**, *244*, 57–62.

(10) Vøllestad, E.; Vigen, C. K.; Magrasó, A.; Haugsrud, R. Hydrogen permeation characteristics of $La_{27}Mo_{1.5}W_{3.5}O_{55.5}$. *J. Membrane Sci.* **2014**, *461*, 81–88.

(11) Chen, Y.; Liao, Q.; Li, Z.; Wang, H.; Wei, Y.; Feldhoff, A.; Caro, J. A CO_2-stable hollow-fiber membrane with high hydrogen permeation flux. *AIChE* **2015**, *61*, 1997–2007.

(12) Polfus, J. M.; Xing, W.; Fontaine, M.-L.; Denonville, C.; Henriksen, P. P.; Bredesen, R. Hydrogen separation membranes based on dense ceramic composites in the $La_{27}W_5O_{55.5}$–$LaCrO_3$ system. *J. Membrane Sci.* **2015**, *479*, 39–45.

(13) Chen, Y.; Cheng, S.; Chen, L.; Wei, Y.; Ashman, P. J.; Wang, H. Niobium and molybdenum co-doped $La_{5.5}WO_{11.25-\delta}$ membrane with improved hydrogen permeability. *J. Membrane Sci.* **2016**, *510*, 155–163.

(14) Zayas-Rey, M. J.; dos Santos-Gómez, L.; Marrero-López, D.; León-Reina, L.; Canales-Vázquez, J.; Aranda, M. A. G.; Losilla, E. R. Structural and conducting features of niobium-doped lanthanum tungstate, $La_{27}(W_{1-x}Nb_x)_5O_{55.55-\delta}$. *Chem. Mater.* **2013**, *25*, 448–456.

(15) Zayas-Rey, M. J.; dos Santos-Gómez, L.; Cabeza, A.; Marrero-López, D.; Losilla, E. R. Proton conductors based on alkaline-earth substituted $La_{28-x}W_{4+x}O_{54+3x/2}$. Dalton Trans. **2014**, *43*, 6490–6499.

(16) Porras-Vázquez, J. M.; dos Santos-Gómez, L.; Marrero-López, D.; Slater, P. R.; Masó, N.; Magrasó, A.; Losilla, E. R. Effect of tri- and tetravalent metal doping on the electrochemical properties of lanthanum tungstate proton conductors. *Dalton Trans.* **2016**, *45*, 3130–3138.

(17) Amsif, M.; Magrasó, A.; Marrero-López, D.; Ruiz-Morales, J. C.; Canales-Vázquez, J.; Núñez, P. Mo-substituted lanthanum tungstate $La_{28-y}W_{4+y}O_{54+\delta}$: a competitive mixed electron–proton conductor for gas separation membrane applications. *Chem. Mater.* **2012**, *24*, 3868–3877.

(18) Shlyakhtina, A. V.; Savvin, S. N.; Lyskov, N. V.; Kolbanev, I. V.; Karyagina, O. K.; Chernyak, S. A.; Shcherbakova, L. G.; Núñez, P. Polymorphism in the Family of $Ln_{6-x}MoO_{12-\delta}$ (Ln= La, Gd - Lu; x=0, 0.5) Oxygen Ion- and Proton-Conducting Materials. *J. Mater. Chem. A.* **2017**, *5*, 7618-7630.

(19) Savvin, S. N.; Avdeev, M.; Kolbanev, I. V.; Kharitonova, E. P.; Shcherbakova, L.G.; Shlyakhtina, A.V.; Nuñez, P. Stability against reduction of fluorite-like rhombohedral $La_{5.5}MoO_{11.25}$ and $Ho_{5.4}Zr_{0.6}MoO_{12.3}$ fluorite: Conductivity and neutron diffraction study. *Solid State Ion.* **2018**, *319*, 148–155.

(20) Schildhammer, D.; Fuhrmann, G.; Petschnig, L.; Penner, S., Kogler, M.; Götsch, T.; Schaur, A.; Weinberger, N.; Saxer, A.; Schottenberger, H.; Huppertz, H. Synthetic Access to Cubic Rare Earth Molybdenum Oxides $RE_6MoO_{12-\delta}$ (RE = Tm–Lu) Representing a New Class of Ion Conductors. *Chem. Mater*. **2016**, *28*, 7487–7495.

(21) Savvin, S. N.; Shlyakhtina, A. V.; Borunova, A. B.; Shcherbakova, L. G.; Ruiz-Morales, J. C.; Núñez, P. Crystal structure and proton conductivity of some Zr-doped rare-earth molybdates. *Solid State Ion*. **2015**, *271*, 91–97

(22) Savvin, S.N.; Shlyakhtina, A.V.; Kolbanev, I.V.; Knotko, A.V.; Belov, D.A.; Shcherbakova, L.G.; Nuñez, P. Zr-doped samarium molybdates — potential mixed electron–proton conductors. *Solid State Ion*. **2014**, *262*, 713–718.

(23) Shlyakhtina, A. V.; Savvin, S. N.; Knotko, A. V.; Shcherbakova, L. G.; Núñez, P. Electrical Conductivity of $Ln_{6-x}Zr_xMoO_{12+\delta}$ (Ln = La, Nd, Sm; x = 0.2, 0.6) Ceramics during Thermal Cycling. *Inor. Mat*. **2016**, 52, 1055-1062.

(24) López-Vergara, A.; Porras-Vázquez, J. M.; Infantes-Molina, A.; Canales-Vázquez, J.; Cabeza, A.; Losilla, E. R.; Marrero-López, D. Effect of Preparation Conditions on the Polymorphism and Transport Properties of $La_{6-x}MoO_{12-\delta}$ ($0 \le x \le 0.8$). *Chem. Mater*. **2017**, *29*, 6966–6975.

(25) X´Pert HighScore Plus Program, Version 3.0e, PANalytical B.V., Amelo, The Netherlands, 2012.

(26) Larson, A. C.; von Dreele, R. B., GSAS Program, Los Alamos National Lab, 1994. Rep. No. LA-UR-86748.

(27) Digital Micrograph™, Version 3.22.1461.0, Gatan.

(28) Abrantes, J. C. C. Estereología, UIDM, ESTG, Polytechnic Institute of Viana do Castelo, Viana do Castelo, Portugal, 1998.

(29) Johnson, D. ZView: a Software Program for IES Analysis, Version 2.8, Scribner Associates, Inc., Southern Pines, NC, 2002.

(30) Norby, T. EMF method determination of conductivity contributions from protons and other foreign ions in oxides. *Solid State Ion*. **1988**, *28-30*, 1586–1591.

(31) Liu, X.; Fan, H.; Li, Q.; Shi, J. Monoclinic Distortion Shrinkage and Enhanced Properties of $La_2Mo_2O_9$ Oxide Ion Conductors Synthesized by an Isobaric-Microwave Assisted Method. *ECS Solid State Letters* **2013** *2 (9)* N27-N30.

(32) Liu, X.; Fan, H.; Shi, J.; Dong G.; Li, Q. High oxide ion conducting solid electrolytes of bismuth and niobium co-substituted $La_2Mo_2O_9$. Int. J. Hyd. Energy **2014**, *39*, 17819-17827.

(33) Battle, P. D.; Catlows, C. R. A.; Moroney, L. M. Structural and Dynamical Studies of δ-Bi_2O_3 Oxide-Ion Conductors. *J. Solid State Chem*. **1987**, *67*, 42–50.

(34) Vannier, R.-N.; Abraham, F.; Nowogrocki, G.; Mairesse, G. New Structural and Electrical Data on Bi-Mo Mixed Oxides with a Structure Based on $[Bi_{12}O_{14}]_\infty$ Columns. *J. Solid State Chem*. **1999**, *142*, 294–304.

(35) Goutenoire, F.; Isnard, O.; Retoux, R.; Lacorre, P. Crystal Structure of $La_2Mo_2O_9$, a New Fast Oxide-Ion Conductor. *Chem. Mater*. **2000**, *12*, 2575–2580.

(36) Corbel, G.; Laligant, Y.; Goutenoire, F.; Suard, E.; Lacorre, P. Effects of Partial Substitution of Mo^{6+} by Cr^{6+} and W^{6+} on the Crystal Structure of the Fast Oxide-Ion Conductor Structural Effects of W^{6+}. *Chem. Mater*. **2005**, *17*, 4678–4684.

(37) Norberg, S. T.; Eriksson, S. G.; Hull, S. Comparison of short-range ion–ion correlations in the α, β and δ phases of Bi_2O_3. *Solid State Ion*. **2011**, *192*, 409–412.

(38) Aldebert, P.; Dianoux, A. J.; Traverse, J. P. Neutron scattering evidence for fast ionic oxygen diffusion in the high temperature phases of La_2O_3. *J. Phys.-Paris* **1979**, *40*, 1005–1012.

(39) Fender, B. E. F. In Chemical Applications of Thermal Neutron Scattering; Willis, B. T. M., Ed.; Oxford University Press: London, 1974; pp 250–270.

(40) Shannon, R. D. Revised Effective Ionic Radii and Systematic Studies of Interatomic Distances in Halides and Chalcogenides. *Acta Crystallogr*. **1976**, *A32*, 751–767.

(41) Hubert, P.H.; Michel, P.; Vincent, C. Structure du molybdite de lanthane $La_3Mo_2O_{10}$. *Comptes Rendus Hebdomadaires des Seances de l'Academie des Sciences, Serie C, Sciences Chimiques* **1969,** *269*, 1287–1289.

(42) Aguadero, A.; Martínez-Lope, M. J.; Pomjakushin, V., Alonso, J. A. Oxygen-Deficient R_2MoO_6-delta (R = Tb, Dy, Y, Ho, Er, Tm, Yb) with Fluorite Structure as Potential Anodes in Solid Oxide Fuel Cells. *Eur. J. Inorg. Chem*. **2011**, *21*, 3226–3231.

(43) Gattow, G. Beitrag zur Kristallchemie des Systems Bi_2O_3-MoO_3. *Zeitschrift fuer Anorganische und Allgemeine Chemie* **1958**, *298*, 64–71.

(44) Schönberg, N. On the existence of a metallic molybdenum oxide. *Acta Chem. Scand*. **1954**, *8*, 617–619.

(45) Malavasi, L.; Kim, H.; Billinge, S. J. L.; Proffen, T.; Tealdi, C.; Flor, G. Nature of the monoclinic to cubic phase transition in the fast oxygen ion conductor $La_2Mo_2O_9$ (LAMOX). *J. Am. Chem. Soc*. **2007**, *129*, 6903-6907.

(46) Minh, N.Q.; Takahashi, T. Science and Technology of Ceramic Fuel Cell, Elsevier, N.Y, 1995.

(47) Ren, P.; Masó, N.; Liu, Y.; Ma, L.; Fan, H.; West, A.R. Mixed oxide ion and proton conduction and p-type semiconduction in $BaTi_{0.98}Ca_{0.02}O_{2.98}$ ceramics. *J. Mater. Chem. C,* **2013**, *1*, 2426–2432.

(48) Porras-Vazquez, J.M.; De la Torre, A.G.; Marrero-López, D.; Losilla, E.R.; Aranda, M.A.G. A new family of oxide ion conductors based on tricalcium oxy-silicate. *Dalton Trans*., **2006**, 2691–2697.

(49) Labrincha, J.A.; Frade, J.R.; Marques, F.M.B. Protonic conduction in $La_2Zr_2O_7$ -based pyrochlore materials, *Solid State Ion*., **1997**, *99*, 33-40.

(50) Labrincha, J.A.; Frade, J.R.; Marques, F.M.B. Defect structure of $SrZrO_3$, Solid State Ion., **1993**, *61*, 71-75.

FOR TABLE OF CONTENTS ONLY:

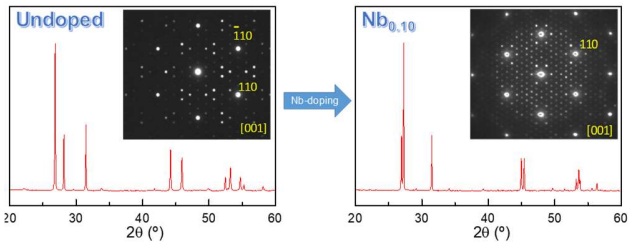

Nb-doping on lanthanum molybdates induces a change in a polymorphism, ascertained both by X-ray diffraction and small angle electron diffraction